nanomaterials

MDPI

Article

Zero- to One-Dimensional Zn_{24} Supraclusters: Synthesis, Structures and Detection Wavelength

Yating Chen [1,2], Zhonghang Chen [1], Jiming Wang [1], Xuandi Ma [1], Linyu Yuan [1], Shuhua Zhang [1,2,*] and Fushun Tang [1,*]

[1] Guangxi Key Laboratory of Electrochemical and Magnetochemical Functional Materials, College of Materials Science and Engineering, Guilin University of Technology, Guilin 541004, China; 1020180460@glut.edu.cn (Y.C.); 1020180495@glut.edu.cn (X.M.)

[2] College of Chemistry, Guangdong University of Petrochemical Technology, Maoming 525000, China

* Correspondence: zsh720108@163.com (S.Z.); tfushun@glut.edu.cn (F.T.)

Abstract: A zinc supracluster $[Zn_{24}(ATZ)_{18}(AcO)_{30}(H_2O)_{1.5}]\cdot(H_2O)_{3.5}$ (**Zn_{24}**), and a 1D zinc supracluster chain $\{[Zn_{24}(ATZ)_{18}(AcO)_{30}(C_2H_5OH)_2(H_2O)_3]\cdot(H_2O)_{2.5}\}_n$ (**1-D⊂Zn_{24}**) with molecular diameters of 2 nm were synthesized under regulatory solvothermal conditions or the micro bottle method. In an N,N-dimethylformamide solution of **Zn_{24}**, Fe^{3+}, Ni^{2+}, Cu^{2+}, Cr^{2+} and Co^{2+} ions exhibited fluorescence-quenching effects, while the rare earth ions Ce^{3+}, Dy^{3+}, Er^{3+}, Eu^{3+}, Gd^{3+}, Ho^{3+}, La^{3+}, Nd^{3+}, Sm^{3+}, and Tb^{3+}showed no obvious fluorescence quenching. In ethanol solution, the **Zn_{24}** supracluster can be used to selectively detect Ce^{3+} ions with excellent efficiency (limit of detection (LOD) = 8.51×10^{-7} mol/L). The **Zn_{24}** supracluster can also detect wavelengths between 302 and 332 nm using the intensity of the emitted light.

Keywords: supracluster; 24 nuclear; fluorescence quenching; detect wavelengths; limit of detection

check for updates

Citation: Chen, Y.; Chen, Z.; Wang, J.; Ma, X.; Yuan, L.; Zhang, S.; Tang, F. Zero- to One-Dimensional Zn_{24} Supraclusters: Synthesis, Structures and Detection Wavelength. *Nanomaterials* **2023**, *13*, 3058. https://doi.org/10.3390/nano13233058

Academic Editors: Antonino Gulino and Josefina Pons

Received: 3 November 2023
Revised: 27 November 2023
Accepted: 27 November 2023
Published: 30 November 2023

1. Introduction

In recent years, polynuclear metal complexes have received considerable attention due to their functional applications in science and technology, exhibiting magnetic [1–4], fluorescence [5–8], optical [9–12], electronic [13], optoelectronic [14] and catalytic properties [15–17]. In addition, they are used in the treatment and diagnosis of various diseases [18,19], as well as in the components of sensors [20–22]. Among the diverse transition-metal polynuclear complexes, zinc complexes show unique properties and variable structural fluorescence [22] and catalytic [15,17] properties. These properties are due to the d^{10} electron shell structure of Zinc(II) that has ideal flexible coordination modes and various coordination numbers. In addition, many aspects of the synthesis affect the structure and nuclear number of transition-metal polynuclear complexes, including the metal ions, ligands, concentrations, counter-ions, templates, solvents, temperatures, and pH [23–25].

The careful selection of an appropriate organic ligand with specific characteristics, such as variable bonding modes and the ability to engage in supramolecular interactions, can facilitate the tailoring and construction of clusters with desirable properties [26–28]. Based on the advantages of abundant coordination modes (Scheme 1), multiple coordination sites, strong binding ability, and a particular orientation [29], tetrazole is desirable for the preparation of metal cluster/cage coordination polymers (CPs) with rich node–linker connectivity, diverse one- through three-dimensionality, specific topological structures, and superior physicochemical properties [30–33]. Among these compounds, nonadecanuclear sliver cluster-based CPs have the highest nuclear number of tetrazolium and its derivatives [34]. Using 5-amino-1,2,3,4-tetrazole (Hatz), we synthesized a zinc supracluster $[Zn_{24}(ATZ)_{18}(AcO)_{30}(H_2O)_{1.5}]\cdot(H_2O)_{3.5}$ (**Zn_{24}**), and a zinc supracluster chain $\{[Zn_{24}(ATZ)_{18}(AcO)_{30}(C_2H_5OH)_2(H_2O)_3]\cdot(H_2O)_3\}_n$ (**1-D⊂Zn_{24}**). To the best of our knowledge, both **Zn_{24}** and **1-D⊂Zn_{24}** are the largest cluster or cluster-based CPs constructed

using tetrazole and its derivatives. In particular, the **Zn$_{24}$** supracluster can detect wavelengths of light in the range of 300–340 nm.

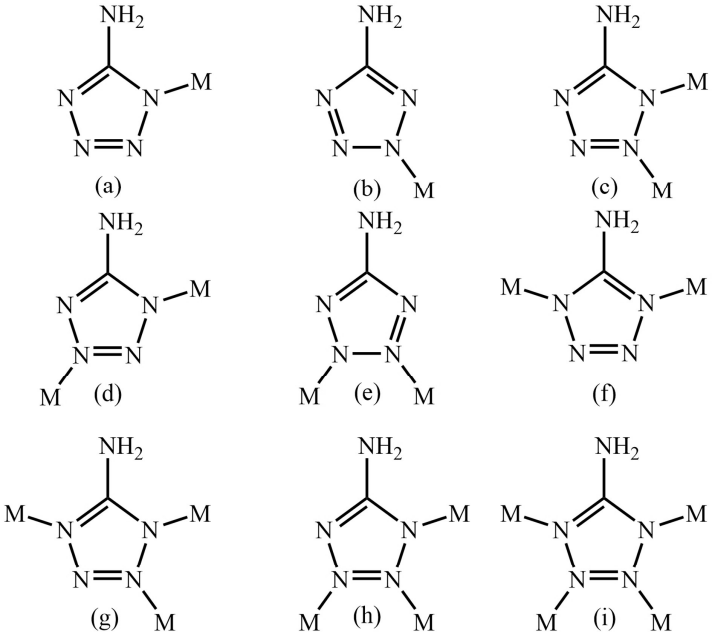

Scheme 1. Coordination modes of Hatz. (**a**) μ_1:1η^1; (**b**) μ_1:1η^2; (**c**) μ_2:1η^1:2η^1; (**d**) μ_2:1η^1:3η^1; (**e**) μ_2:2η^1:3η^1; (**f**) μ_2:1η^1:4η^1; (**g**) μ_3:1η^1:2η^1:4η^1; (**h**) μ_3:1η^1:2η^1:3η^1; (**i**) μ_4:1η^1:2η^1:3η^1:4η^1.

2. Experimental Methodology

2.1. Materials and Physical Measurements

All chemicals were bought commercially and used directly after receipt. Elemental analyses were performed using a Perkin-Elmer 240 elemental analyzer (CHN). The FT-IR spectra were captured in the 4000–400 cm^{-1} region from KBr pellets on a Bio-Rad FTS-7 spectrometer. The SHELXL crystallographic program for molecular structures was used to determine the X-ray crystal structures using an Agilent G8910A CCD diffractometer. Photoluminescence experiments were performed using a Hitachi F-4600 fluorescence spectrophotometer. The power X-ray diffraction (PXRD) patterns were determined using a PANalytical X'Pert^3 power diffractometer (operating at 40 kV and 40 mA) with graphite-monochromatized Cu Kα radiation (λ = 1.54056 Å). ^{1}H NMR spectra were recorded on Bruker AVANCE III 500 instruments.

2.2. Synthesis of L^1H_2–L^5H_2

A mixture of 5-amino-1,2,3,4-tetrazole (Hatz) (10 mmol), salicylaldehyde derivatives (10 mmol), and ethanol (20 mL) was refluxed at 353 K for 1 h in a 100 mL flask. A beige precipitate of L^nH_2 formed, and it was then rinsed three times with fresh ethanol (10 mL × 3) and dried at 50 °C for 24 h (refer to the ESI† for details).

2.3. Synthesis of Zn_{24}

A mixture of H_2L^1 (0.5 mmol, 0.1340 g), $Zn(CH_3COO)_2{\cdot}2H_2O$ (0.5 mmol, 0.1048 g), and ethanol (10 mL) was stirred for 30 min, with the pH adjusted to 6 through the addition of triethylamine. The mixture was then sealed in a 15 mL Teflon-lined stainless-steel vessel, and heated at 353 K for 48 h in an oven, followed by slow cooling to room temperature. Four-cornered golden yellow crystals in a double-cone shape were collected, washed with ethanol, and dried in air. Phase-pure **Zn$_{24}$** crystals were obtained through manual separation (yield: 66.5 mg, ca. 64.33% based on Zn(II)). *Anal. Calc.* for **Zn$_{24}$**: $C_{78}H_{138}N_{90}O_{66}Zn_{24}$ (*M*r = 4961.66), *calc.*: C, 18.88; H, 2.80; N, 25.39%. Found: C, 18.79; H, 2.87; N, 25.46%. The FT-IR data for **Zn$_{24}$** (Figure S1, KBr, cm^{-1}) were as follows: 3445 s, 1578 m, 1400 w, 1165 w, 1101 m, 941 w, 758 w, 685 w, 616 w, and 483 w.

2.4. Synthesis of 1-D⊂Zn_{24}

A mixture of H_2L^1 (0.5 mmol, 0.1340 g), $Zn(CH_3COO)_2{\cdot}2H_2O$ (0.5 mmol, 0.1048 g), ethanol (10 mL) and acetonitrile (2 mL) was stirred for 30 min with the pH adjusted to 6 through the addition of triethylamine. The mixture was then sealed in a 20-mL micro bottle capable of autonomously adjusting the reaction pressure and heated at 343 K for 48 h. Subsequently, the micro bottle was slowly cooled to room temperature. Four-cornered golden yellow crystals with a double-cone shape were collected, washed with ethanol and dried in air. Phase-pure crystals of **1-D⊂Zn$_{24}$** were obtained through manual separation (yield: 70.2 mg, ca. 66.67% based on Zn(II)). *Anal. Calc.* for **1-D⊂Zn$_{24}$**: $C_{82}H_{150}N_{90}O_{68}Zn_{24}$ (*M*r = 5053.79), *calc.*: C, 19.01; H, 2.99; N, 24.93%. Found: C, 18.92; H, 3.06; N, 25.04%. The FT-IR data for **Zn$_{24}$** (Figure S1, KBr, cm^{-1}) were as follows: 3445 s, 1578 m, 1400 w, 1165 w, 1101 m, 941 w, 758 w, 685 w, 616 w, and 483 w.

2.5. Single-Crystal X-ray Diffraction

The single-crystal data of the **Zn$_{24}$** and **1-D⊂Zn$_{24}$** complexes were collected using a SuperNova (single source at offset) Eos with graphite monochromatic Mo-Kα radiation (λ = 0.71073 Å) in the ω scan mode in the ranges of $3.16° \leq \theta \leq 25.01°$ and $3.30° \leq \theta \leq 25.01°$, respectively. Raw frame data were integrated using the SAINT program [35]. The **Zn$_{24}$** and **1-D⊂Zn$_{24}$** structures were solved with direct methods using SHELXS [35] and refined with full-matrix least-squares on F^2 using SHELXL-2018 within the Olex2 GUI [36]. Empirical absorption correction using spherical harmonics was implemented in the SCALE3 ABSPACK scaling algorithm. All non-hydrogen atoms were refined anisotropically. All hydrogen atoms to carbon atoms were positioned geometrically and refined as riding atoms. Calculations and graphics were performed with *SHELXTL* [35]. The computer programs used in this study were CrysAlis PRO (Agilent Technologies, Version 1.171.37.35 released 13-08-2014 CrysAlis171.NET compiled 13 August 2014), SHELXL [35], and Olex2 [36]. The crystallographic details of **Zn$_{24}$** and **1-D⊂Zn$_{24}$** are provided in Table 1. Selected bond lengths and angles for **Zn$_{24}$** and **1-D⊂Zn$_{24}$** are listed in Tables S1 and S2.

Table 1. Crystallographic data for **Zn$_{24}$** and **1-DZn$_{24}$**.

Complexes	Zn$_{24}$	1-D⊂Zn$_{24}$
Formula	$C_{78}H_{138}N_{90}O_{66}Zn_{24}$	$C_{82}H_{150}N_{90}O_{68}$ Zn_{24}
Formula weight	4961.66	5053.79
Crystal system	Monoclinic	triclinic
Crystal size (mm)	0.25 × 0.21 × 0.16	0.21 × 0.18 × 0.13
Space group	$P2_1/n$	$P\bar{1}$
a (Å)	20.264(1)	16.718(1)
b (Å)	23.996(1)	17.449(1)
c (Å)	21.663(1)	19.054(1)
α (°)	90.00	70.651(3)
β (°)	108.738(4)	80.304(3)
γ (°)	90.00	70.651(3)
V (Å^3)	9975.3(6)	5062.8(3)
F(000)	4968	2536
Z	2	1
D_c (g cm^{-3})	1.646	1.658
μ (mm^{-1})	2.917	2.877
θ range (°)	3.16, 25.01	3.30,25.01
Ref. meas./indep.	74,768, 17,433	39,347, 17,765
Obs. ref. [$I > 2\sigma(I)$]	11,953	11,553
R_{int}	0.0520	0.0473
R_1 [$I \geq 2\sigma$ (I)] [a]	0.0600	0.0673
ωR_2(all data) [b]	0.1934	0.2037
Goof	1.039	1.041
$\Delta\rho$(max, min) (e Å^{-3})	1.001, −0.867	1.126, −0.694

[a] $R_1 = \Sigma||F_o| - |F_c||/\Sigma|F_o|$. [b] $wR_2 = [\Sigma w(|F_o^2| - |F_c^2|)^2/\Sigma w(|F_o^2|)^2]^{1/2}$.

3. Results and Discussion

3.1. Structural and Synthetic Details

Herein, we investigated the effects of ligand, reaction temperature, counterbalance anion, ligand/metal ion molar ratio, solvent, and synthetic method on the self-assembly of supraclusters (Scheme 2). The synthetic strategy for the Hatz system is depicted in Scheme 2. First, a mixture of $Zn(OAc)_2{\cdot}2H_2O$ (0.2 mmol), 4-bromo-2-[(1H-tetrazol-5-ylimino)-methyl]-phenol (**H_2L^1**, 0.2 mmol), and anhydrous ethanol (10 mL) was poured into a Teflon-lined autoclave (20 mL). The autoclave was cooled slowly to room temperature after heating at 80 °C for 2 days. Four-cornered golden yellow **Zn_{24}** crystals in a double-cone shape were collected via filtration. In the **Zn_{24}** supracluster, Hatz is produced by the decomposition of **H_2L^1**. To understand the role of **H_2L^1** in the synthesis, we used various salicylaldehyde-derived Schiff bases (**H_2L^2-H_2L^5**) instead of 4-bromo-2-[(1H-tetrazol-5-ylimino)-methyl]-phenol (**H_2L^1**) to conduct the same experiment, but we could not obtain the **Zn_{24}** supercluster or analog. Similarly, if only **H_2L^1** was replaced by Hatz, the **Zn_{24}** supercluster or analog was not obtained. Through previous experiments, we can draw the conclusion that although 5-bromosalicylicaldehyde does not participate in coordination in the 24-atom Zn cluster, 5-bromosalicylicaldehyde is an essential raw material for the synthesis of the **Zn_{24}** cluster. Thus, we speculate that 5-bromosalicylicaldehyde may act as a template.

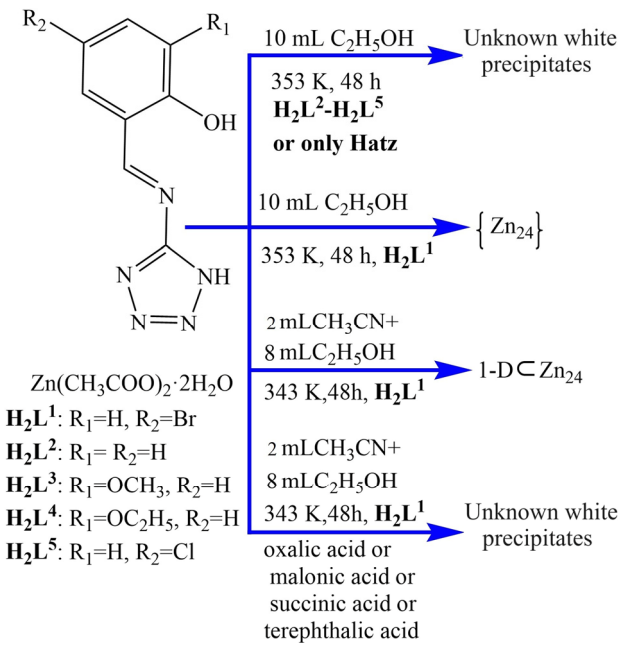

Scheme 2. Regulatory process of **Zn_{24}** and **1-D⊂Zn_{24}**.

According to the ring structure of **Zn_{24}**, the **Zn_{24}** cluster can form a 1D chain or 2D network through bridging ligands. **H_2L^1** and $Zn(CH_3COO)_2{\cdot}2H_2O$ were selected as the starting materials. By tuning the reaction temperature, solvent, ligand/metal salt molar ratio, and synthetic methods, the optimal synthesis conditions for the 1D Zn supracluster chain **1-D⊂Zn_{24}** were determined as follows: reaction temperature, 70 °C; solvent, anhydrous ethanol (8 mL), and acetonitrile (2 mL); **H_2L^1**/$Zn(CH_3COO)_2{\cdot}2H_2O$ molar ratio, 2:1; and reactor, micro bottle (autonomously adjusting the reaction pressure).

To obtain a 2D supracluster network, we replaced acetic acid with various carboxylic acids such as oxalic acid, malonic acid, succinic acid, and terephthalic acid. However, these experiments were unsuccessful.

3.2. Crystal Structures of Zn_{24} and 1-D⊂Zn_{24}

Single crystal analysis confirmed **Zn_{24}** to have a 0D wheel-like coordination supracluster of the monoclinic crystal system with $P2_1/n$ space group consisting of 24 Zn^{II} atoms, 30 acetate groups, 1.5 coordinated water molecules, 3.5 lattice water molecules and 18 Atz ligands derived from H_2L^1 (Figure 1a). The Zn_{24} cluster was stabilized by 5-amino-1,2,3,4-tetrazole, which binds along the wheel of the cluster core (Figure 1b), bridging the four neighboring zinc atoms. Acetate groups further stabilized the cluster through 18 μ_2:η^1:η^1-acetate bridging two zinc atoms. The 12 Zn ions in the inner ring of the wheel (inner red ring shown in Figure 1a) coordinated with four N atoms from four different Atz ligands and two O atoms from two *syn-syn*-μ_2:η^1:η^1-acetate bridging groups to form a distorted octahedral geometry. By contrast, the 12 Zn atoms in the outer ring (outer red ring shown in Figure 1a) coordinated with two N atoms from two different Atz ligands. They also coordinated with two or three O atoms from one *syn-syn*-μ_2:η^1:η^1-acetate bridging group and one μ_1:η^1:η^1-acetate terminal group or one μ_1:η^1-acetate ligand, as well as one coordinated water molecule, to form a distorted tetragonal pyramidal, or a trigonal bipyramidal or an octahedral geometry. Close inspection of the nanosized wheel-like conformation showed approximate wheel dimensions of 8.912 × 20.491 × 9.747 Å (inner ring diameter × outer ring diameter × wheel thickness), where the inner ring diameter is the distance between tetrazole planes (i.e., planes (N31,N32,N33,N34,C27) and (N31, N32, N33, N34, C27)^i, symmetry code: (i)-*x*,-*y*,-*z*); the outer ring diameter is N30⋯N30^i; and the wheel thickness is the distance between the C13-C29^i-C26^i -plane and the C13^i-C29-C26-plane.

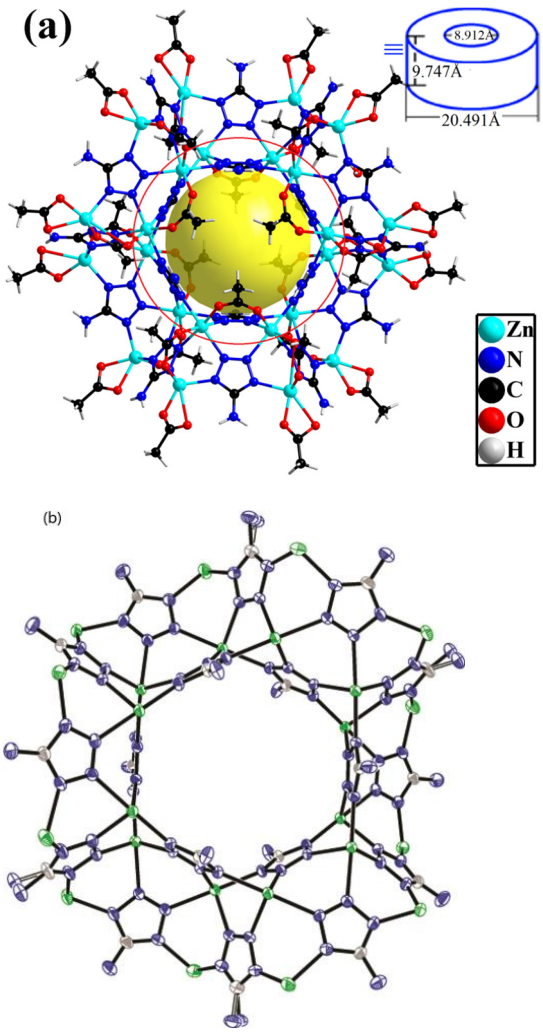

Figure 1. (**a**) Crystal structure of **Zn_{24}**. (**b**) Zinc Atz core.

Complexes **1-D⊂Zn$_{24}$** and **Zn$_{24}$** have similar basic structures, i.e., the **Zn$_{24}$** supracluster. Complex **1-D⊂Zn$_{24}$** was constructed as a 1D Zn_{24} suprachain through the double *syn-anti-* μ_2:η^1:η^1-bridging acetic group linking of Zn_{24} (Figure 2).

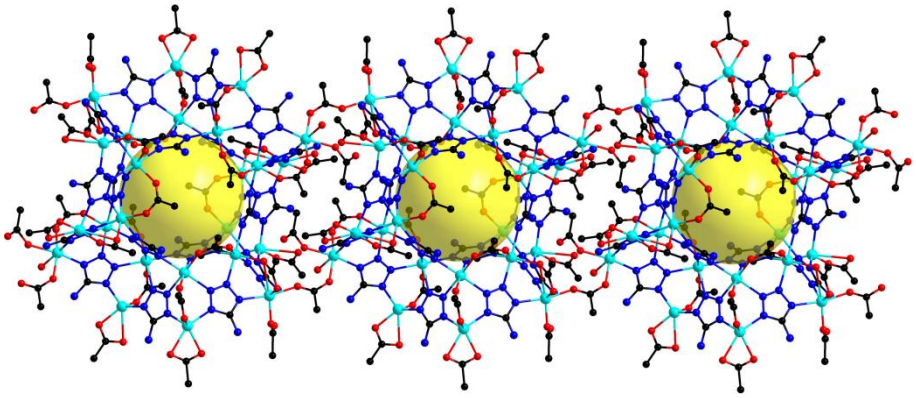

Figure 2. 1D chain of **1-D⊂Zn$_{24}$**.

3.3. Luminescent Properties

Numerous studies have demonstrated the good fluorescence of clusters, especially those of Zn(II) and Cd(II) ions with closed d subshells [37,38]. In recent years, Zn(II) clusters have been widely used in luminescent probes due to their desirable advantages in detection and promising applications in biological and environmental systems [39]. Luminescent probes and complexes can selectively detect various sizes of molecules or ions through their adjustable porosity [40].

In this paper, the luminescent properties (the phase purity of **Zn$_{24}$** has been checked using PXRD patterns, Figure S7) of **Zn$_{24}$** were investigated in different solvents with concentrations of 1×10^{-6} mol·L^{-1} (Figure 3). Upon photoexcitation at 404, 382, 426 and 418 nm in water, N,N-dimethylformamide (DMF), DMSO, and ethanol solvent, **Zn$_{24}$** exhibited green, blue, green and green luminescent emission bands with fluorescence maxima at 496, 459, 507, and 508 nm, respectively. These results predominantly originated from the metal-to-ligand charge-transfer excited state [41,42]. Furthermore, **Zn$_{24}$** exhibited a qualitative change in its luminescence due to the interaction between metal ions and ligands, and it had a stronger fluorescence intensity in DMF and ethanol solutions. Although **Zn$_{24}$** also had a stronger fluorescence intensity in DMSO, we did not consider DSMO for **Zn$_{24}$** luminescent probes due to its high toxicity. Thus, we discussed the **Zn$_{24}$** complex as a luminescent probe for highly selective sensing in DMF and ethanol.

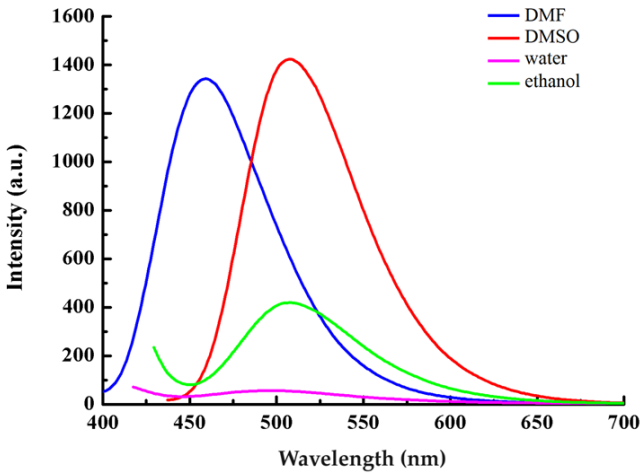

Figure 3. Luminescence of **Zn$_{24}$** in different solutions.

Zn$_{24}$ (1 mg) was immersed in 10 mL of DMF solutions containing MCl_n (M = Al^{3+}, Ba^{2+}, Co^{2+}, Cr^{2+}, Cu^{2+}, Fe^{3+}, Mn^{2+}, Ni^{2+}, Pb^{2+}, or Zn^{2+}) to form complex suspensions incorporating various metal ions for luminescence studies, and Fe^{3+}, Ni^{2+}, Cu^{2+}, Cr^{2+}, and Co^{2+} ions all demonstrated a fluorescence-quenching effect (Figure 4), indicating that **Zn$_{24}$** was not selective toward ions in DMF solution. At the same time, the rare earth ions (Ce^{3+}, Dy^{3+}, Er^{3+}, Eu^{3+}, Gd^{3+}, Ho^{3+}, La^{3+}, Nd^{3+}, Sm^{3+}, and Tb^{3+}) have no clear fluorescence-quenching effects (Figure S3). However, **Zn$_{24}$** showed high selectivity in ethanol solution. The luminescence intensity of **Zn$_{24}$** revealed that the addition of Ce^{3+} can lead to complete quenching in ethanol solution compared with other metal ions (Figure 5).

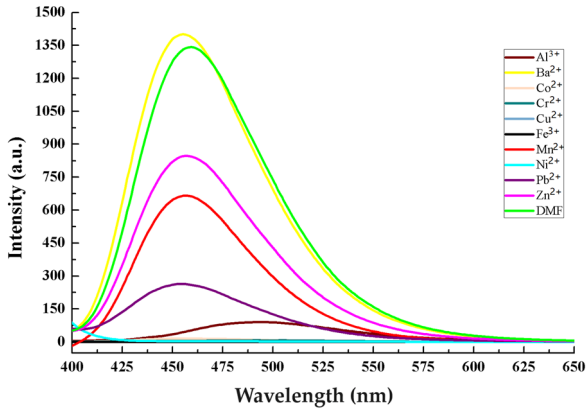

Figure 4. Liquid-state fluorescence behavior of **Zn$_{24}$** in DMF.

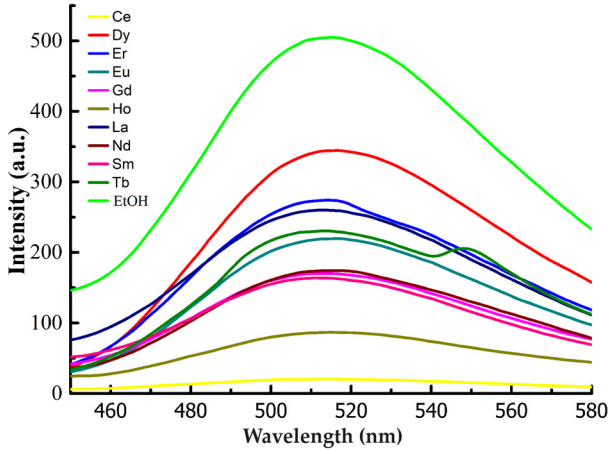

Figure 5. Liquid-state fluorescence behavior of **Zn$_{24}$** in ethanol.

The **Zn$_{24}$** (1 mg, with a final concentration of 1 mg/mL in ethanol) and different concentrations of Ce^{3+} (from 1×10^{-2} to 1×10^{-8} mol/L) were added to the sample tube at room temperature. The fluorescence spectrum was taken at its excitation wavelength (λ = 402 nm).

The fluorescence spectra of the Zn_{24}-Ce^{3+} system for various concentrations of Ce^{3+} are shown in Figure 6. The fluorescence intensity at 504 nm progressively increased as the concentration of Ce^{3+} decreased. In addition, we quantitatively analyzed the quenching efficiency through the Stern–Volmer equation: $I_o/I = K_{sv}[C] + 1$, where I_o and I are the respective emission intensities before and after adding Ce^{3+}, while C is the concentration of Ce^{3+} in ethanol solution. The quenching efficiency, of **Zn$_{24}$** was $-1.68 \times 10\ M^{-1}$ (Figure S5). According to the limit of detection (LOD) = $3\delta/K_{sv}$ (Figure S6), we calculated an LOD of 8.51×10^{-7} mol/L, which was lower than the reported LOD of the Ln-MOF [41].

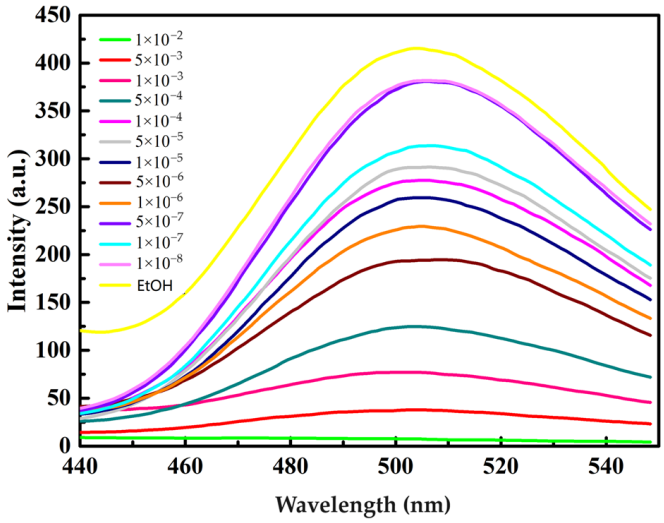

Figure 6. Liquid-state fluorescence behavior of **Zn$_{24}$** for different concentrations of Ce^{3+} in ethanol.

3.4. Detection Wavelength

The solid-state fluorescence spectra of Hatz were obtained at a slit width of 5 nm and an excitation wavelength of 402 nm, while the solid-state fluorescence spectra of **Zn$_{24}$** were obtained at an excitation wavelength of 302–332 nm (Figure 7 and Figure S4). Under the same test conditions, the fluorescence spectrum of Hatz peaked at 615 nm, while that of **Zn$_{24}$** peaked at 502 nm. The luminous color changed from red to blue–green, and the fluorescence intensity of **Zn$_{24}$** was more than 200 times that of Hatz. The full-type Zn^{2+} metal ion in **Zn$_{24}$** has an extra-nuclear d^{10} electron, and did not undergo a d–d transition, leading to a significant enhancement in luminous intensity. At the same time, the deprotonated tetrazolium ring is an electron-deficient conjugated ring that causes the electron migration (M→L) of zinc ions to the tetrazolium ring [42,43]. As a result, the luminous color changed from red to blue–green, and the fluorescence intensity of **Zn$_{24}$** was more than 200 times that of Hatz. The fluorescence intensity of **Zn$_{24}$** decreased linearly with the increase in excitation wavelength (Figures 7 and 8). Between 302 and 332 nm, the wavelength of the excitation light can be determined by detecting the intensity of the emitted light.

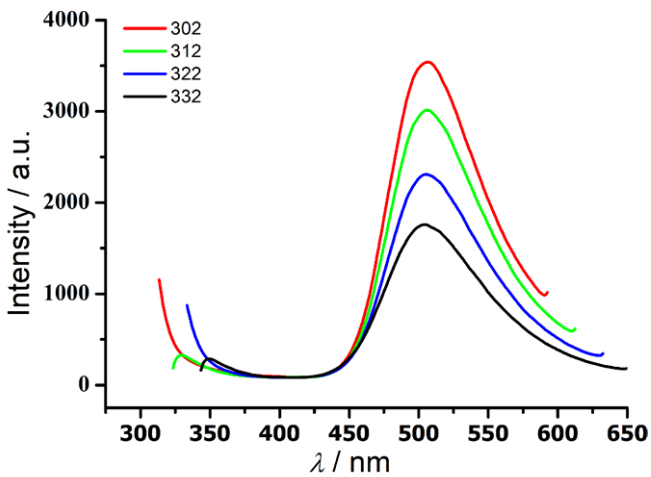

Figure 7. Solid-state emission spectra of **Zn$_{24}$** under 302, 312, 322 and 332 nm excitation at room temperature.

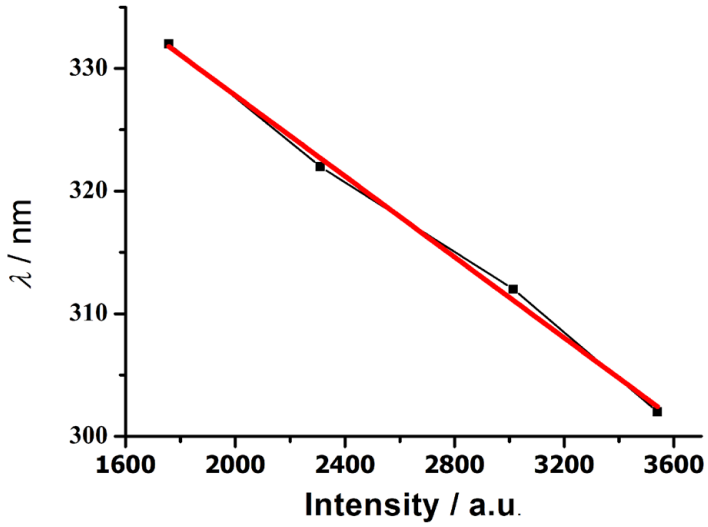

Figure 8. Fluorescence intensity (a.u.) vs. wavelength of excitation light (nm).

3.5. Hirshfeld Surface Analysis of the Complex ***Zn*$_{24}$**

Hirshfeld surface analysis [44] is a useful tool for describing the surface characteristics of molecules, and was performed to visualize the different intermolecular interactions in crystal structures by employing 3D molecular surface contours. Figure 9 displays the findings of the **Zn$_{24}$** Hirshfeld surface study. The middle shape index ranges from −1.000 to 1.000 Å, whereas the range of the d_{norm} surface on the left is −1.238 to 1.570 Å. The range of the curvature curvedness was −4.000 to 0.400 Å. In Figure 9, the d_{norm} surface map of **Zn$_{24}$** is colored from light to dark red spots to represent the interaction force of the complex **Zn$_{24}$** from weak to strong.

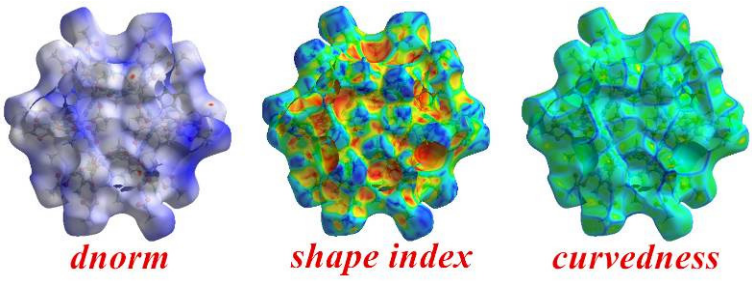

Figure 9. Hirshfeld surface mapped with d_{norm} (**left**), shape index (**middle**), and curvedness (**right**) for complex **Zn$_{24}$**.

One useful supplement for Hirshfeld surface analysis is the 2-D fingerprint plot [45]. It quantitatively analyses the nature and type of intermolecular interaction between the molecules inside the crystals. The fingerprint plots can be decomposed to highlight particularly close contacts between the elements (Figure 10). The H···H interaction is one of the most significant contacts for the **Zn$_{24}$** complex.

The main intermolecular interaction of **Zn$_{24}$** is H···H contact, which is reflected in the middle of the scattered points of the 2-D fingerprint plots (the percentage of H···H contacts of **Zn$_{24}$** is 40.4%). Another main intermolecular interaction of **Zn$_{24}$** is O···H interaction, which is represented by double spikes in the bottom left (acceptor and donor) region of the fingerprint plots. Accordingly, we can infer that there are significant N-H···O hydrogen bonds (Table S3) observed in **Zn$_{24}$** (the percentage of O···H contacts of **Zn$_{24}$** is 22.4%). Also, the N···H contacts play important roles for **Zn$_{24}$**. The percentage of N···H contacts of **Zn$_{24}$** is 10.0%. In addition to those above, the presence of C···H, C···O, and N···O contacts were also observed. These three forces accounted for 4.0%, 1.4% and 1.3% of the total Hirshfeld surface force, respectively.

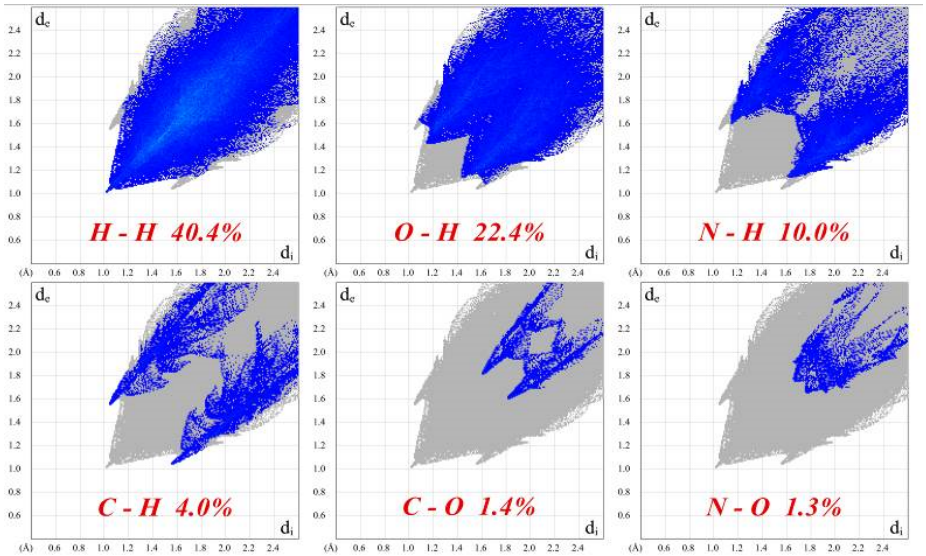

Figure 10. Fingerprint plots of complex **Zn$_{24}$**.

4. Conclusions

A supracluster zinc, **Zn$_{24}$**, and a zinc supracluster 1D chain, **1-D⊂Zn$_{24}$**, were synthesized through regulatory solvothermal reactions. In an ethanol solution, **Zn$_{24}$** was synthesized at 353 K using a solvothermal method, whereas **1-D⊂Zn$_{24}$** was formed when a mixed solution (2 mL acetonitrile + 8 mL ethanol) was used at 343 K using a micro bottle. The **Zn$_{24}$** supracluster can be used to selectively detect Ce^{3+} with excellent efficiency (LOD = 8.51×10^{-7} mol/L), and can be used as a potential sensor for their detection. In addition, the **Zn$_{24}$** supracluster can detect wavelengths between 302 and 332 nm, using the intensity of emitted light. Thus, the **Zn$_{24}$** supracluster can potentially be used as a spectral detection material to prepare optical wave detectors.

Supplementary Materials: The following supporting information can be downloaded at: https://www.mdpi.com/article/10.3390/nano13233058/s1, Figure S1: IR of H_2L^1-H_2L^5; Figure S2: IR of **Zn24**; Figure S3: The liquid-state fluorescence behaviors of Zn24 in DMF; Figure S4: Emission spectra of HATZ in a solid state at 402 nm excitation wavelength at room temperature; Figure S5: The fitting curve of the luminescence intensity of **Zn$_{24}$** at different Ce^{3+} concentration; Figure S6: The fluorescence spectra of blank **Zn$_{24}$** (1 mg·mL^{-1}) at different measurements; Figure S7: XRD of the complex **Zn$_{24}$**; Table S1: Selected bond lengths (Å) and angles (°) for **Zn$_{24}$**; Figure S8: ^{1}H NMR (400 MHz, DMSO-d$_6$) for **L^{1}H$_2$**; Figure S9: ^{1}H NMR (400 MHz, DMSO-d$_6$) for **L^{2}H$_2$**; Figure S10: ^{1}H NMR (400 MHz, DMSO-d$_6$) for **L^{3}H$_2$**; Figure S11: ^{1}H NMR (400 MHz, DMSO-d$_6$) for **L^{4}H$_2$**; Figure S12: ^{1}H NMR (400 MHz, DMSO-d$_6$) for **L^{5}H$_2$**; Table S2: Selected bond lengths (Å) and angles (°) for **1-D⊂Zn$_{24}$**; Table S3: Hydrogen bond lengths (Å) and angles (°) for **Zn$_{24}$.**

Author Contributions: Y.C., Z.C. and J.W.: designed and supervised the project and experiments; Y.C., Z.C., J.W., X.M. and L.Y. performed the data analysis and prepared the manuscript; S.Z., and F.T.: provided resources and acquired funding; and S.Z. and F.T. provided academic guidance. All authors have read and agreed to the published version of the manuscript.

Funding: This research was funded by the National Natural Science Foundation of China (No. 21861014), and by the Talent Introduction Program of Guangdong Institute of Petrochemical Technology (No. 2020RC033).

Data Availability Statement: The data presented in this study are available in this article and Supplementary Material.

Conflicts of Interest: The authors declare that they have no conflict of interest to report regarding the present study.

References

1. Bao, S.S.; Zheng, L.M. Magnetic materials based on 3d metal phosphonates. *Coord. Chem. Rev.* **2016**, *319*, 63–85. [CrossRef]
2. Han, S.D.; Zhao, J.P.; Liu, S.J.; Bu, X.H. Hydro(solvo)thermal synthetic strategy towards azido/formato-mediated molecular magnetic materials. *Coord. Chem. Rev.* **2016**, *289–290*, 32–48.
3. Kitchen, J.A. Lanthanide-based self-assemblies of 2, 6-pyridyldicarboxamide ligands: Recent advances and applications as next-generation luminescent and magnetic materials. *Coord. Chem. Rev.* **2017**, *340*, 232–246. [CrossRef]
4. Ashebr, T.G.; Li, H.; Ying, X.; Li, X.-L.; Zhao, C.; Liu, S.; Tang, J. Emerging trends on designing high-performance dysprosium (III) single-molecule magnets. *ACS Mater. Lett.* **2022**, *4*, 307–319. [CrossRef]
5. Liu, J.Q.; Luo, Z.-D.; Pan, Y.; Singh, A.K.; Trivedi, M.; Kumar, A. Recent developments in luminescent coordination polymers: Designing strategies, sensing application and theoretical evidences. *Coord. Chem. Rev.* **2020**, *406*, 213145. [CrossRef]
6. Zhou, Q.; Ren, G.; Yang, Y.; Wang, C.; Che, G.; Li, M.; Yu, M.-H.; Li, J.; Pan, Q. Fluorescence Thermometers Involving Two Ranges of Temperature: Coordination Polymer and DMSP Embedding. *Inorg. Chem.* **2023**, *62*, 16652–16658. [CrossRef] [PubMed]
7. Yang, Z.; Xu, T.; Li, H.; She, M.; Chen, J.; Wang, Z.; Zhang, S.; Li, J. Zero-Dimensional Carbon Nanomaterials for Fluorescent Sensing and Imaging. *Chem. Rev.* **2023**, *123*, 11047–11136. [CrossRef]
8. Zhang, C.; Qin, Y.; Ke, Z.; Yin, L.; Xiao, Y.; Zhang, S. Highly efficient and facile removal of As (V) from water by using Pb-MOF with higher stable and fluorescence. *Appl. Organomet. Chem.* **2023**, *37*, e7066. [CrossRef]
9. Suess, R.J.; Winnerl, S.; Schneider, H.; Helm, M.; Berger, C.; De Heer, W.A.; Murphy, T.E.; Mittendorff, M. Role of transient reflection in graphene nonlinear infrared optics. *Acs Photonics* **2016**, *3*, 1069–1075. [CrossRef]
10. Gwo, S.; Sun, L.; Li, X.; Chen, H.-Y.; Lin, M.-H. Nanomanipulation and controlled self-assembly of metal nanoparticles and nanocrystals for plasmonics. *Chem. Soc. Rev.* **2016**, *45*, 5672–5716. [CrossRef]
11. Gwo, S.; Wang, C.Y.; Chen, H.Y.; Lin, M.H.; Sun, L.; Li, X.; Chen, W.L.; Chang, Y.M.; Ahn, H. Plasmonic metasurfaces for nonlinear optics and quantitative SERS. *ACS Photonics* **2016**, *3*, 1371–1384. [CrossRef]
12. Yang, X.G.; Zhai, Z.M.; Lu, X.M.; Ma, L.F.; Yan, D. Fast crystallization-deposition of orderly molecule level heterojunction thin films showing tunable up-conversion and ultrahigh photoelectric response. *ACS Cent. Sci.* **2020**, *6*, 1169–1178. [CrossRef] [PubMed]
13. Lee, S.W.; Choi, B.J.; Eom, T.; Han, J.H.; Kim, S.K.; Song, S.J.; Lee, W.; Hwang, C.S. Influences of metal, non-metal precursors, and substrates on atomic layer deposition processes for the growth of selected functional electronic materials. *Coord. Chem. Rev.* **2013**, *257*, 3154–3176. [CrossRef]
14. Zhao, Y.X.; Yang, G.; Lu, X.M.; Yang, C.D.; Fan, N.N.; Yang, Z.T.; Wang, L.Y.; Ma, L.F. {Zn6} Cluster based metal–organic framework with enhanced room-temperature phosphorescence and optoelectronic performances. *Inorg. Chem.* **2019**, *58*, 6215–6221. [CrossRef] [PubMed]
15. Pang, J.Y.; Gao, Q.; Yin, L.; Zhang, S.H. Synthesis and catalytic performance of banana cellulose nanofibres grafted with poly (ε-caprolactone) in a novel two-dimensional zinc (II) metal-organic framework. *Int. J. Biol. Macromol.* **2023**, *224*, 568–577. [CrossRef] [PubMed]
16. Liu, J.; Yang, G.P.; Jin, J.; Wu, D.; Ma, L.F.; Wang, Y.Y. A first new porous d–p HMOF material with multiple active sites for excellent CO_2 capture and catalysis. *Chem. Commun.* **2020**, *56*, 2395–2398. [CrossRef] [PubMed]
17. Wu, Y.P.; Tian, J.W.; Liu, S.; Li, B.; Zhao, J.; Ma, L.F.; Li, D.S.; Lan, Y.Q.; Bu, X. Bi-Microporous metal–organic frameworks with cubane [M4 (OH) 4](M= Ni, Co) clusters and pore-space partition for electrocatalytic methanol oxidation reaction. *Angew. Chem. Int. Ed.* **2019**, *58*, 12185–12189. [CrossRef]
18. Baig, M.M.F.A.; Ma, J.; Gao, X.; Khan, M.A.; Ali, A.; Farid, A.; Zia, A.W.; Noreen, S.; Wu, H. Exploring the robustness of DNA nanotubes framework for anticancer theranostics toward the 2D/3D clusters of hypopharyngeal respiratory tumor cells. *Int. J. Biol. Macromol.* **2023**, *236*, 123988. [CrossRef]
19. Zhivkova, T.; Culita, D.C.; Abudalleh, A.; Dyakova, L.; Mocanu, T.; Madalan, A.M.; Georgieva, M.; Miloshev, G.; Hanganu, A.; Marinescu, G.; et al. Homo-and heterometallic complexes of Zn (ii),{Zn (ii) Au (i)}, and {Zn (ii) Ag (i)} with pentadentate Schiff base ligands as promising anticancer agents. *Dalton Trans.* **2023**, *52*, 12282–12295. [CrossRef]
20. Zhang, Y.; Yuan, S.; Day, G.; Wang, X.; Yang, X.; Zhou, H.C. Luminescent sensors based on metal-organic frameworks. *Coord. Chem. Rev.* **2018**, *354*, 28–45. [CrossRef]
21. Yu, C.X.; Hu, F.L.; Song, J.G.; Zhang, J.L.; Liu, S.S.; Wang, B.X.; Meng, H.; Liu, L.; Ma, L.F. Ultrathin two-dimensional metal-organic framework nanosheets decorated with tetra-pyridyl calix [4] arene: Design, synthesis and application in pesticide detection. *Sens. Actuat. B-Chem.* **2020**, *310*, 127819. [CrossRef]
22. Wang, S.T.; Zheng, X.; Zhang, S.H.; Li, G.; Xiao, Y. A study of GUPT-2, a water-stable zinc-based metal–organic framework as a highly selective and sensitive fluorescent sensor in the detection of Al^{3+} and Fe^{3+} ions. *CrystEngComm* **2021**, *23*, 4059–4068. [CrossRef]
23. Avila, R.J.; Emery, D.J.; Pellin, M.J.; Martinson, B.F.A.; Farha, K.O.; Hupp, T.J. Porphyrins as Templates for Site-Selective Atomic Layer Deposition: Vapor Metalation and in Situ Monitoring of Island Growth. *ACS Appl. Mater Inter.* **2016**, *8*, 19853–19859. [CrossRef] [PubMed]
24. Gao, P.; Ma, H.; Wu, Q.; Qiao, L.; Volinsky, A.A.; Su, Y.J. Size-dependent vacancy concentration in nickel, copper, gold, and platinum nanoparticles. *Phys. Chem. C* **2016**, *120*, 17613–17619. [CrossRef]

25. Kumar, R.; Kaur, N.; Kaur, R.; Kaur, N.; Sahoo, S.C.; Nanda, P.K. Temperature controlled synthesis and transformation of dinuclear to hexanuclear zinc complexes of a benzothiazole based ligand: Coordination induced fluorescence enhancement and quenching. *J. Mol. Struct.* **2022**, *1265*, 133300. [CrossRef]
26. Islam, S.; Tripathi, S.; Hossain, A.; Seth, S.K.; Mukhopadhyay, S.J. pH-induced structural variations of two new Mg (II)-PDA complexes: Experimental and theoretical studies. *J. Mol. Struct.* **2022**, *1265*, 133373. [CrossRef]
27. Feng, C.; Zhu, Y.Q.; Huang, H.H.; Zhao, H.J. A Triazolate-Supported $Fe_3(\mu_3\text{-O})$ Core: Crystal Structure, Fluorescence, and Hirshfeld Surface Analysis. *J. Clust. Sci.* **2016**, *27*, 1181–1190. [CrossRef]
28. Sebastian, S.; Tim, S.; Mariam, B.; Jan, V.L.; Arif, N.M.; Paul, K.G. A planar decanuclear cobalt (II) coordination cluster. *Inorg. Chim. Acta* **2018**, *482*, 522–525.
29. Gaponik, P.N.; Voitekhovich, S.V.; Ivashkevich, O.A. Metal derivatives of tetrazoles. *Russ. Chem. Rev.* **2010**, *37*, 507–603.
30. Li, J.R.; Yu, Q.; Sañudo, E.C.; Tao, Y.; Bu, X.H. An azido–Cu^{II}–triazolate complex with utp-type topological network, showing spin-canted antiferromagnetism. *Chem. Commun.* **2007**, *25*, 2602–2604. [CrossRef]
31. Tong, X.L.; Hu, T.L.; Zhao, J.P.; Wang, Y.K.; Zhang, H.; Bu, X.H. Chiral magnetic metal–organic frameworks of MnII with achiral tetrazolate-based ligands by spontaneous resolution. *Chem. Commun.* **2010**, *46*, 8543–8545. [CrossRef]
32. Bai, Y.; Dou, Y.; Xie, L.H.; Rutledge, W.; Li, J.R.; Zhou, H.C. Zr-based metal–organic frameworks: Design, synthesis, structure, and applications. *Chem. Soc. Rev.* **2016**, *45*, 2327. [CrossRef] [PubMed]
33. Kang, X.M.; Tang, M.H.; Yang, G.L.; Zhao, B. Cluster/cage-based coordination polymers with tetrazole derivatives. *Coord. Chem. Rev.* **2020**, *422*, 213424. [CrossRef]
34. Liang, M.X.; Ruan, C.Z.; Sun, D.; Kong, X.J.; Ren, Y.P.; Long, L.S.; Huang, R.B.; Zheng, L.S. Solvothermal synthesis of four polyoxometalate-based coordination polymers including diverse Ag (I) $\cdot$ π interactions. *Inorg. Chem.* **2014**, *53*, 897–902. [CrossRef] [PubMed]
35. Sheldrick, G.M. Crystal structure refinement withSHELXL. *Acta Cryst.* **2015**, *A71*, 3–8. [CrossRef] [PubMed]
36. Dolomanov, O.V.; Bourhis, L.J.; Gildea, R.J.; Howard, J.A.K.; Puschmann, H.J. OLEX2: A complete structure solution, refinement and analysis program. *Appl. Cryst.* **2009**, *42*, 339–341. [CrossRef]
37. Wei, G.H.; Yang, J.; Ma, J.F.; Liu, Y.Y.; Li, S.L.; Zhang, L.P. Syntheses, structures and luminescent properties of zinc (II) and cadmium (II) coordination complexes based on new bis (imidazolyl) ether and different carboxylate ligands. *Dalton Trans.* **2008**, *23*, 3080–3092. [CrossRef]
38. Su, Z.; Fan, J.; Okamura, T.A.; Chen, M.S.; Chen, S.S.; Sun, W.Y. Interpenetrating and self-penetrating zinc (II) complexes with rigid tripodal imidazole-containing ligand and benzenedicarboxylate. *Cryst. Growth Des.* **2010**, *10*, 1911–1922. [CrossRef]
39. Tian, Y.; Wang, Y.; Xu, Y.; Liu, Y.; Li, D.; Fan, C. A highly sensitive chemiluminescence sensor for detecting mercury (II) ions: A combination of Exonuclease III-aided signal amplification and graphene oxide-assisted background reduction. *Sci. China Chem.* **2015**, *58*, 514–518. [CrossRef]
40. Gao, W.Y.; Chrzanowski, M.; Ma, S. Metal–metalloporphyrin frameworks: A resurging class of functional materials. *Chem. Soc. Rev.* **2015**, *45*, 1602–1608. [CrossRef]
41. Zhang, Q.; Wang, J.; Kirillov, A.M.; Dou, W.; Xu, C.; Xu, C.; Yang, L.; Fang, R.; Liu, W. Multifunctional Ln–MOF luminescent probe for efficient sensing of Fe^{3+}, Ce^{3+}, and acetone. *ACS Appl. Mater. Inter.* **2018**, *10*, 23976–23986. [CrossRef]
42. Chen, Y.; Yang, T.; Pan, H.; Yuan, Y.; Chen, L.J. Photoemission mechanism of water-soluble silver nanoclusters: Ligand-to-metal–metal charge transfer vs strong coupling between surface plasmon and emitters. *J. Am. Chem. Soc.* **2014**, *136*, 1686–1689. [CrossRef]
43. Huo, P.; Hou, J.; Lei, Z.; Chen, Q.-Y.; Dai, T. Ligand-to-ligand charge transfer within metal–organic frameworks based on manganese coordination polymers with tetrathiafulvalene-bicarboxylate and bipyridine ligands. *Inorg. Chem.* **2016**, *55*, 6496–6503. [CrossRef] [PubMed]
44. Spackman, M.A.; Jayatilaka, D. Hirshfeld surface analysis. *CrystEngComm* **2009**, *11*, 19–32. [CrossRef]
45. Sama, F.; Ansari, L.A.; Raizada, M.; Ahmad, M.; Nagaraja, C.M.; Shahid, M.; Kumar, A.; Khan, K.; Siddiqi, Z.A. Design, structures and study of non-covalent interactions of mono-, di-, and tetranuclear complexes of a bifurcated quadridentate tripod ligand, N-(aminopropyl)-diethanolamine. *New. J. Chem.* **2017**, *41*, 1959–1972. [CrossRef]